

# Permanent Magnet Temperature Distribution Estimation in Permanent Magnet Synchronous Machines Using Back Electromotive Force Harmonics

David Reigosa<sup>1</sup>, Daniel Fernandez<sup>1</sup>, Tsutomu Tanimoto<sup>2</sup>, Takashi Kato<sup>2</sup>, Fernando Briz<sup>1</sup>

<sup>1</sup>University of Oviedo. Department of Electrical, Computer & System Engineering. <sup>2</sup> Nissan Motor Co., Ltd, Nissan Research Center, EV System Laboratory.

[diazdavid@uniovi.es](mailto:diazdavid@uniovi.es), [fernandezalodaniel@uniovi.es](mailto:fernandezalodaniel@uniovi.es), [tanimoto-t@mail.nissan.co.jp](mailto:tanimoto-t@mail.nissan.co.jp), [katou-t@mail.nissan.co.jp](mailto:katou-t@mail.nissan.co.jp), [fernando@isa.uniovi.es](mailto:fernando@isa.uniovi.es)

**Abstract:** PM temperature measurement/estimation in permanent magnet synchronous machines (PMSMs) is convenient both for torque control and monitoring purposes. Most of existing methods provide an averaged/punctual temperature. However, PM temperature distribution is not uniform, which can have unexpected adverse effects like reduced accuracy estimating the torque produced by the machine or local demagnetization e.g. due to hot spots. PM temperature distribution can be measured or estimated. Inner and outer PM surfaces are not visible once the machine is assembled. Therefore measurement of the PM temperature distribution cannot be realized by visual means. An array of temperature sensors attached to the PM can be used in this case. While this is technically feasible, it is unaffordable in commercial products due to cost and robustness issues. Alternatively, the PM temperature distribution can be estimated. The paper analyzes the use of back electromotive force (BEMF) harmonics to estimate the differential temperature in the PM of a PMSM, i.e. the temperature difference between the hottest and coldest parts of the magnets. Combined with average PM temperature estimation methods, this information can be used to estimate the PM temperature spatial distribution. The proposed method has been developed on an empirical basis.<sup>1</sup>

**Index Terms** — Permanent magnet synchronous machines, magnet temperature estimation, high frequency signal injection, back-emf.

## I. Introduction

Temperature estimation in PMSM has been the focus of significant research efforts during the last years [1-9]. An increase of the PM temperature reduces the PM strength [5-7], adversely impacting the torque production capability of the machine. Furthermore, the PMs can be permanently demagnetized if the PM temperature becomes too high [5-7]. PM temperature measurement/estimation is desirable therefore both for torque control and monitoring purposes [4-7, 9].

PM temperature measurement in PMSMs is not trivial. Contact-type temperature sensors normally used to measure the stator temperature in electric machines (e.g. PTC thermistors), are not easy to mount on the rotor, as this would require cabling to a rotating part through slip rings and brushes [5, 6]. The use of thermocouples combined with a wireless transmission system has already been proposed [7]. However, this solution places cost and robustness concerns. Non-contact sensors, i.e. infrared (IR) [5, 6], can also be used. However, they are relatively

expensive. In addition, this solution requires that the magnet surface is visible, which can be viable in most SPMSMs designs [5, 6], but not in IPMSMs designs [7]. In all the cases, the use of either contact-type or non contact-type temperature sensors, compromise the machine robustness and increases the system cost. Due to this, PM temperature measurement is not normally implemented in standard machines.

Alternative to direct measurement, PM temperature can be estimated. PM temperature estimation methods can be divided into thermal models [2, 3, 10-15], BEMF based methods [16-19, 21, 24, 25] and methods based on the injection of some form of test signal [5-9]. Thermal models are usually based on a 2D model of the machine, assuming therefore a uniform spatial PM temperature distribution along the magnet (i.e. in the axial direction). These methods can be potentially extended to 3D, but at the price of a significant increase of the model complexity [15]. In all the cases, thermal models require precise knowledge of the machine geometry, materials and cooling system, the model being specific therefore for each machine design. BEMF based methods estimate the magnet temperature from the estimated PM flux linkage [16-19], while methods based on the injection of a high frequency signal, estimate the magnet temperature from the stator reflected magnet high frequency resistance [5-7]. Both methods provide a lumped temperature, but with no information on the PM temperature spatial distribution.

As already mentioned, PMs of PMSMs are subject to irreversible demagnetization if their temperature becomes too high [5-7]. Demagnetization can be global [20], when the temperature in the PM is uniform, or partial (local) when the spatial temperature distribution is not uniform [20]. Consequently, estimation not only of the average temperature, but also of the maximum PM temperature, can be crucial to prevent partial demagnetization of the PMs. Additionally, estimation of the spatial temperature distribution can be used to compensate its effects on the torque ripple in the machine.

This paper analyzes the effects of a non-uniform magnet temperature distribution on the BEMF harmonics, and its use to estimate the magnet differential temperature. The magnet differential temperature, combined with the average PM temperature can be used to estimate the spatial temperature distribution. The proposed method has been developed on an empirical basis; a mathematical model is currently being developed.

The paper is organized as follows: a brief review of PM temperature estimation methods is presented in section II.

<sup>1</sup> This work was supported by Nissan motor Co. Ltd..

Estimation of the mean magnet temperature, as well as discussion on the use of BEMF harmonics to estimate a non-uniform magnet temperature distribution, is presented in Section III. The equipment developed for the measurement of the magnet temperature distribution is presented in section IV. Finally, experimental results confirming the viability of the method are presented in section V.

## II. Review of temperature estimation based methods

Existing methods for PM temperature estimation in PMSMs are reviewed this section, as they will be basis for the method proposed in this work.

### a) *PM temperature estimation using thermal models*

PMSM thermal models consist of thermal nodes that represent uniform temperature regions. The thermal nodes are connected by thermal resistances that represent the heat transfer. Power sources are used to represent the machine power losses (i.e. magnet, copper and core losses) and heat capacitors that represent the heat storage characteristic of the different parts of the machine [10-14]. Thermal models require therefore precise knowledge of the machine geometry, materials and cooling system of the machine, being therefore difficult to obtain. Alternatively, simplified thermal models can be built without previous knowledge of the machine geometry, materials or cooling system, by estimating the machine thermal coefficients during a commissioning process [11, 14].

In addition to the complexity due to the machine geometry, both axial and radial heat transfer and room heat convection needs to be considered. In fan-cooled machines, modeling the room heat convection makes the model dependent on the ambient conditions (room temperature, pressure, humidity...). Consequently, the model needs to be adjusted for each specific machine and placement in this case. In most of the cases, axial heat transfer is not considered, what results in a 2D thermal model [10-14]. While simpler, these models cannot predict a non-uniform PM temperature distribution in the axial direction.

### b) *PM temperature estimation using signal injection*

Methods based on the injection of a test signal (e.g. voltage pulses or a periodic high frequency voltage/current), estimate the magnet temperature from measurable electrical variables (stator voltages and currents). In the method described in [9-10], a voltage pulse was injected in the  $d$ -axis, the resulting stator current depending on the magnetization level, which is function of the temperature. The methods described in [5-7] injected periodic high frequency signals. A rotating voltage was used in [5, 6], while pulsating  $d$ -axis current and pulsating  $d$ -axis voltage and  $q$ -axis current cancellation were proposed in [7]. It was shown in these works that rotating voltage injection is suitable only for SPMSMs, also being sensitive to  $d$  and  $q$ -axis inductances variation as well as to the machine speed. On the contrary, pulsating  $d$ -axis current [7] and pulsating  $d$ -axis voltage and  $q$ -axis current cancellation are insensitive to the speed and inductances variation; also they can be used both with SPMSMs and IPMSMs. Pulsating  $d$ -axis high frequency current injection can be considered therefore superior and will be used in the discussion following. The basics of this method are briefly presented

following as it will be used later in sections III and V for magnet temperature distribution estimation. The basis of the temperature estimation using the high frequency resistance can be found in the Appendix. Detailed discussion can be also found in [7].

The high frequency model of a PMSM expressed in the synchronous rotor reference frame is described by (1), where  $\vec{V}_{dqhf}^r$  and  $\vec{i}_{dqhf}^r$  are the stator voltage and current complex vectors in the rotor synchronous reference frame,  $R_{dhrf}$ ,  $R_{qhrf}$ ,  $L_{dhrf}$  and  $L_{qhrf}$  are the  $d$  and  $q$ -axis resistances and inductances respectively,  $\omega_r$  is the machine speed,  $\lambda_{pm}$  is the PM flux and  $p$  is the differential operator.

If a sinusoidal high frequency current is injected in the  $d$ -axis of a PMSM (IPMSM or SPMSM), with the high frequency  $q$ -axis current being controlled to be zero (2), the resulting stator high frequency voltage,  $\vec{V}_{dqhf}^*$ , is described by (3). The voltage complex vector  $\vec{V}_{dqhf}^r$ , (4), is defined as the  $d$ -axis component of  $\vec{V}_{dqhf}^*$ . Both (2) and (4) can be expressed as (5)-(6), positive sequence ( $\vec{i}_{dqhfpc}^r$  and  $\vec{V}_{dqhfpc}^*$ ) and negative sequence ( $\vec{i}_{dqhfnrc}^r$  and  $\vec{V}_{dqhfnrc}^*$ ) components are observed. The  $d$ -axis impedance (7) can be obtained from (5) and (6), were  $\varphi_{zd}$ , (8), is the phase of the  $d$ -axis PMSM high frequency impedance (7). The overall  $d$ -axis resistance (7) is split into the stator and rotor contributions  $R_{dhrf(T_s)}$  and  $R_{drhf(T_r)}$  (9), the magnet temperature being finally obtained from (10). It is noted that  $T_r$  is a lumped temperature, i.e. it does not provide any information of the spatial temperature distribution.

A drawback of this method is the need to inject a high frequency signal. However, it has the advantage that only knowledge of two machine parameters, i.e.  $\alpha_{cu}$  and  $\alpha_{mag}$ , is required.

$$\begin{bmatrix} \vec{V}_{dhrf}^r \\ \vec{V}_{qhrf}^r \end{bmatrix} = \begin{bmatrix} R_{dhrf} & 0 \\ 0 & R_{qhrf} \end{bmatrix} \begin{bmatrix} \vec{i}_{dhrf}^r \\ \vec{i}_{qhrf}^r \end{bmatrix} + p \begin{bmatrix} L_{dhrf} & 0 \\ 0 & L_{qhrf} \end{bmatrix} \begin{bmatrix} \vec{i}_{dhrf}^r \\ \vec{i}_{qhrf}^r \end{bmatrix} + \begin{bmatrix} 0 & -\omega_r L_{qhrf} \\ \omega_r L_{dhrf} & 0 \end{bmatrix} \begin{bmatrix} \vec{i}_{dhrf}^r \\ \vec{i}_{qhrf}^r \end{bmatrix} \quad (1)$$

$$\vec{i}_{dqhf}^{r*} = \begin{bmatrix} \vec{i}_{dhrf}^{r*} \\ \vec{i}_{qhrf}^{r*} \end{bmatrix} = \begin{bmatrix} I_{hf}^* \cos(\omega_{hf} t) \\ 0 \end{bmatrix} \quad (2)$$

$$\vec{V}_{dqhf}^* = \begin{bmatrix} \vec{V}_{dhrf}^* \\ \vec{V}_{qhrf}^* \end{bmatrix} = \begin{bmatrix} (R_{dhrf} + j\omega_{hf} L_{dhrf}) \vec{i}_{dhrf}^r \\ \omega_r L_{dhrf} \vec{i}_{dhrf}^r \end{bmatrix} \quad (3)$$

$$\vec{V}_{dqhf}^r = \begin{bmatrix} \vec{V}_{dhrf}^* \\ 0 \end{bmatrix} = \begin{bmatrix} (R_{dhrf} + j\omega_{hf} L_{dhrf}) I_{hf}^* \cos(\omega_{hf} t) \\ 0 \end{bmatrix} = \begin{bmatrix} V_{dqhf}^r \cos(\omega_{hf} t + \varphi_{zd}) \\ 0 \end{bmatrix} \quad (4)$$

$$\vec{i}_{dqhf}^{r*} = \frac{I_{hf}}{2} e^{j\omega_{hf} t} + \frac{I_{hf}}{2} e^{-j\omega_{hf} t} = \vec{i}_{dqhfpc}^{r*} + \vec{i}_{dqhfnrc}^{r*} \quad (5)$$

$$V_{dqhf}^{r'} = \frac{|V_{dqhf}^{r'}|}{2} e^{j(\omega_{hf}t - \varphi_{Zd})} + \frac{|V_{dqhf}^{r'}|}{2} e^{j(-\omega_{hf}t + \varphi_{Zd})} =$$

$$V_{dqhfpc}^{r'} + V_{dqhfnc}^{r'}$$

$$Z_d = R_{dqhf} + j\omega_{hf}L_{dqhf} = \frac{V_{dqhfpc}^{r'}}{i_{dqhfpc}^{r'}} = \frac{V_{dqhfnc}^{r'}}{i_{dqhfnc}^{r'}} \quad (7)$$

$$\varphi_{Zd} = \tan^{-1}\left(\frac{\omega_{hf}L_{dqhf}}{R_{dqhf}}\right) \quad (8)$$

$$R_{dqhf(T_s, T_r)} = Z_d \cos(\varphi_{Zd}) = R_{dqhf(T_s)} + R_{dqhf(T_r)} =$$

$$R_{dqhf(T_0)}(1 + \alpha_{cu}(T_s - T_0)) + R_{dqhf(T_0)}(1 + \alpha_{mag}(T_r - T_0)) \quad (9)$$

$$T_r = \frac{R_{dqhf(T_s, T_r)} - R_{dqhf(T_0)}(1 + \alpha_{cu}(T_s - T_0)) - R_{dqhf(T_0)}}{R_{dqhf(T_0)}\alpha_{mag}} + T_0 \quad (10)$$

### c) PM temperature estimation using the BEMF

BEMF based methods estimate the magnet temperature from the PM flux linkage ( $\lambda_{pm}$ ), which is obtained from the machine terminal voltages and currents [16-19, 21, 24, 25]. While obtaining the PM flux linkage from the stator terminals when  $I_d=I_q=0$  is relatively simple, it becomes challenging when either  $I_d$  or  $I_q$  are different from zero. Knowledge of several machine parameters is needed in this case (i.e.  $d$  and  $q$ -axis inductance maps with  $i_{dq}^r$ ) [16-19], increasing the parameter sensitivity of the method. On the other hand, no additional signal needs to be injected.

The fundamental model of a PM machine in the synchronous rotor reference frame is described by (11), where  $V_{dq}$  and  $i_{dq}^r$  are the stator voltage and current complex vectors in the rotor synchronous reference frame,  $R_d$ ,  $R_q$ ,  $L_d$  and  $L_q$  are the  $d$  and  $q$ -axis resistances and inductances respectively,  $\omega_r$  is the machine speed,  $\lambda_{pm}$  is the PM flux and  $p$  is the differential operator.

$$\begin{bmatrix} V_d \\ V_q \end{bmatrix} = \begin{bmatrix} R_d & 0 \\ 0 & R_q \end{bmatrix} \begin{bmatrix} i_d^r \\ i_q^r \end{bmatrix} + p \begin{bmatrix} L_d & 0 \\ 0 & L_q \end{bmatrix} \begin{bmatrix} i_d^r \\ i_q^r \end{bmatrix} + \begin{bmatrix} 0 & -\omega_r L_q \\ \omega_r L_d & 0 \end{bmatrix} \begin{bmatrix} i_d^r \\ i_q^r \end{bmatrix} + \begin{bmatrix} 0 \\ \lambda_{pm} \omega_r \end{bmatrix} \quad (11)$$

Since the PM flux,  $\lambda_{pm}$ , is only present in the  $q$ -axis equation of the machine (11), only the  $q$ -axis voltage equation (12) is needed. In (12),  $R_q$  is function of the stator temperature,  $T_s$ ,  $\lambda_{pm}$  is function of the magnet temperature,  $T_r$ , while  $L_d$  and  $L_q$  are both function of the rotor temperature,  $T_r$ , and of the  $d$  and  $q$ -axis currents  $i_{dq}^r$ . Consequently (12) can be transformed to (13),  $\lambda_{pm}$  being obtained as (14). If it is assumed that  $i_{dq}^r = 0$ , the PM flux can be obtained from (15). The PM flux variation with the magnet temperature can be expressed as (16), where  $T_0$  is the room temperature and  $\beta$  is the magnet flux thermal coefficient. Finally, the magnet temperature,  $T_r$ , can be obtained using (17). As for high frequency signal injection methods, the estimated temperature is a lumped value, not providing therefore information on its spatial distribution.

$$V_q^r = R_q^r i_q^r + pL_q^r i_q^r + \omega_r L_d^r i_d^r + \lambda_{pm} \omega_r \quad (12)$$

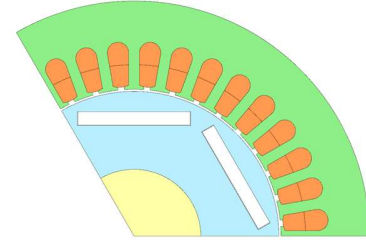


Fig. 1.- IPMSM

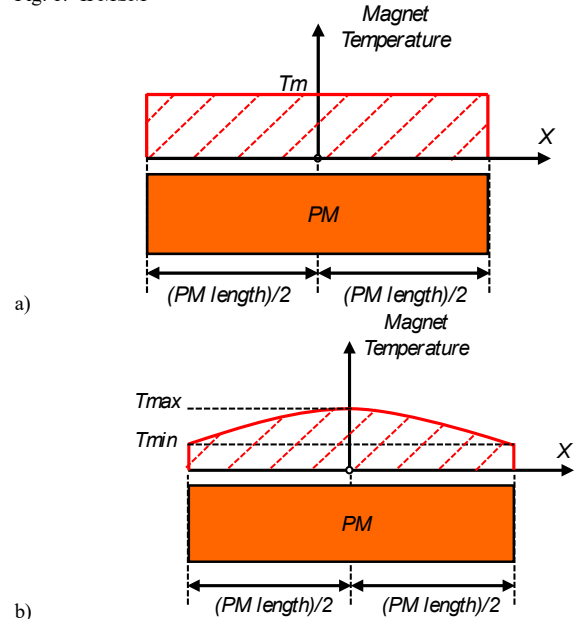


Fig. 2.- Magnet temperature distribution, a) uniform and b) non-uniform.

$$V_q^r = R_{q(T_s)} i_q^r + pL_{q(T_r, i_d^r, i_q^r)} i_q^r + \omega_r L_{d(T_r, i_d^r, i_q^r)} i_d^r + \lambda_{pm(T_r)} \omega_r \quad (13)$$

$$\lambda_{pm(T_r)} = \frac{V_q^r - \left( R_{q(T_s)} i_q^r + pL_{q(T_r, i_d^r, i_q^r)} i_q^r + \omega_r L_{d(T_r, i_d^r, i_q^r)} i_d^r \right)}{\omega_r} \quad (14)$$

$$\lambda_{pm(T_r)} = \frac{V_q^r}{\omega_r} \quad (15)$$

$$\lambda_{pm(T_r)} = \lambda_{pm(T_0)} [1 + \beta(T_r - T_0)] \quad (16)$$

$$T_r = \frac{1}{\beta} \left[ \frac{\lambda_{pm(T_r)}}{\lambda_{pm(T_0)}} - 1 \right] + T_0 \quad (17)$$

### III. Estimation of the magnet temperature distribution

Fig. 1 shows the IPMSM design that will be used both for simulation and experimental verification. The uniform and non-uniform temperature profiles considered are shown in Fig. 2a and Fig. 2b respectively. For the non-uniform temperature distribution, a quadratic law (18) was found to adequately fit with the temperature distribution experimentally measured [7]. The PM dimensions in (18) are indicated in Fig. 2, where  $T_{min}$ ,  $T_{max}$  and  $T_r$  are the minimum, maximum and mean PM temperature respectively, and  $PM_{length}$  is the PM length. Same unskewed design was used for the simulation machine (see Fig. 1) and the test machine. It has been experimentally found that the same

Uniform magnet temperature distribution		Non-uniform magnet temperature distribution			
Cases	$T_r(^{\circ}\text{C})$	Cases	$T_{max}(^{\circ}\text{C})$	$T_{min}(^{\circ}\text{C})$	$T_r(^{\circ}\text{C})$
#1	100	#1	100	100	100
#2	90	#2	100	90	94
#3	80	#3	100	80	88
#4	70	#4	100	70	82
#5	60	#5	100	60	76
#6	50	#6	100	50	70
	--	#7	100	40	64
	--	#8	100	30	58

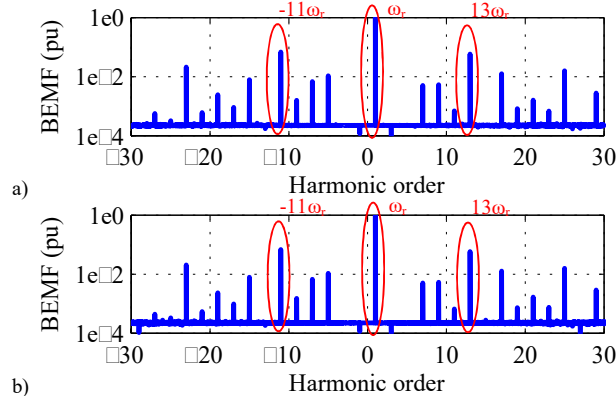


Fig. 3.- Simulation results. BEMF frequency spectrum. a) Uniform magnet temperature distribution and b) non-uniform magnet temperature distribution.  $\omega_r=2*\pi*50$  rad/s.

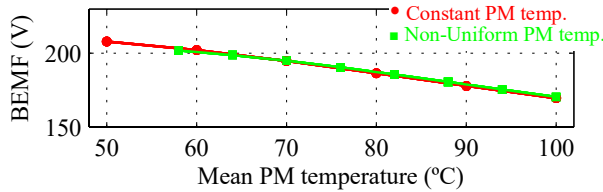


Fig. 4.- Simulation results. Fundamental component of the BEMF vs. mean magnet temperature.  $I_d=I_q=0$  pu and  $\omega_r=2*\pi*50$  rad/s.

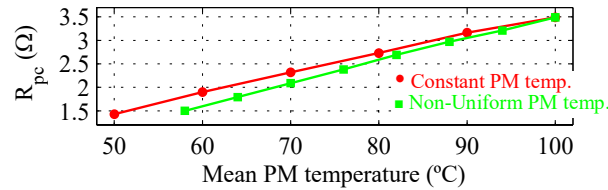


Fig. 5.- Simulation results. Estimated  $d$ -axis high frequency resistance. Pulsating  $d$ -axis high frequency current injection,  $\omega_{hf}=2*\pi*250$  rad/s,  $I_{hf}=0.05$  pu.  $I_d=I_q=0$  pu and  $\omega_r=2*\pi*50$  rad/s.

quadratic law, (18), adequately holds both for tangential and axial temperature distributions.

$$T_{magnet} = \frac{T_{min} - T_{max}}{(PM_{length}/2)^2} X^2 + T_{max} = \frac{T_{min} - T_{max}}{(PM_{length}/2)^2} X^2 + \left( T_r + \frac{T_{max} - T_{min}}{3} \right) \quad (18)$$

To obtain the magnet temperature distribution using (18), the mean PM temperature  $T_r$  and the differential PM temperature  $T_{min}-T_{max}$  need to be estimated. Methods to do this are discussed following.

#### a) Mean magnet temperature estimation ( $T_r$ )

This subsection evaluates the mean PM temperature estimation. Use of the BEMF (17) and of a pulsating  $d$ -axis high frequency current signal injection (10) are discussed, both for the case of uniform and non-uniform temperature distributions. Finite element analysis (FEA) will be used for this analysis [15]. Table I shows the temperature profiles used for simulation. The stator temperature is kept constant for all the simulations. The machine is fed by a linear source, no distortion of the voltage due to the PWM strategy or a non-ideal behavior of the inverter exists therefore.

Fig. 3 shows the FFT of the BEMF for the cases of a uniform and a non-uniform magnet temperature distributions (see Table I). The results are normalized in pu with respect to the 1<sup>st</sup> harmonic of the BEMF. A logarithmic scale is used for the magnitudes. The harmonic content is the same for uniform and non-uniform temperature distributions, harmonic magnitudes being slightly different. Three components of interest are observed:  $\omega_r$ ,  $13\omega_r$  and  $-11\omega_r$  harmonics.

Fig. 4 shows the magnitude variation of the 1<sup>st</sup> harmonic of the BEMF (component at  $\omega_r$ , 50Hz), and which corresponds to  $V_q$  in (15), as the mean magnet temperature changes,  $T_r$  (see Table I). As predicted by (15)-(16), its magnitude decreases as the mean magnet temperature increases. It is observed that the same BEMF magnitude is induced both for the cases of a uniform and a non-uniform magnet temperature distributions. It is therefore concluded that the 1<sup>st</sup> harmonic of the BEMF does not contain information on the magnet temperature distribution. However, it can be used for mean PM temperature estimation.

Fig. 5 shows the estimated rotor  $d$ -axis high frequency resistance,  $R_{drift(T_r)}$  (9), when a pulsating  $d$ -axis high frequency current is injected, both for the cases of a uniform and a non-uniform magnet temperature distribution, its magnitude decreasing as the mean magnet temperature decreases, see (9). It is also observed that the estimated  $d$ -axis high frequency resistance variation with the mean PM temperature is higher for the non-uniform magnet temperature distribution case compare to the uniform temperature distribution case. This means that different PM temperatures would be estimated for the same PM high frequency resistance, inducing therefore an error in the estimated temperature. This variation could be potentially used to estimate the differential magnet temperature  $T_{min}-T_{max}$ . This is an ongoing research issue.

#### b) Differential magnet temperature estimation ( $T_{min}-T_{max}$ )

This subsection analyzes differential PM temperature estimation using the BEMF harmonics. Simulation details are the same as for mean PM temperature estimation. Fig. 3 shows the frequency spectrum of the BEMF, three components of interest are observed:  $\omega_r$ ,  $13\omega_r$  and  $-11\omega_r$ . As discussed in previous subsection, the component at  $\omega_r$  does not contain information of the differential PM temperature; however, it can be used to estimate the mean PM temperature. On the contrary,  $13\omega_r$  and  $-11\omega_r$  harmonics can be used for PM differential temperature estimation, this is analyzed following.

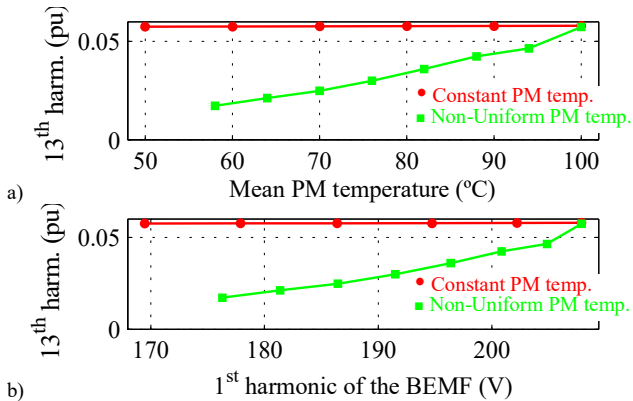


Fig. 6.- Simulation results. BEMF 13<sup>th</sup> harmonic magnitude vs. mean magnet temperature, a), and vs. the 1<sup>st</sup> harmonic magnitude of the BEMF, b).  $\omega_r = 2\pi \cdot 50$  Hz.

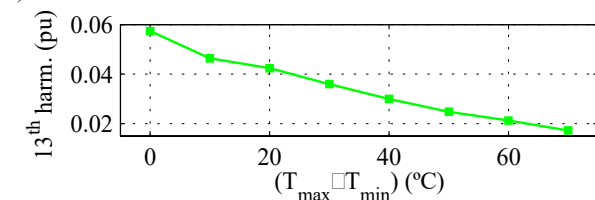


Fig. 7.- Simulation results. BEMF 13<sup>th</sup> harmonic magnitude vs. differential magnet temperature, i.e.  $(T_{max} - T_{min})$ .  $\omega_r = 2\pi \cdot 50$  Hz.

Fig. 6a shows the magnitude of the BEMF 13<sup>th</sup> harmonic (see Fig. 3), as a function of the mean magnet temperature, while Fig. 6b shows the same harmonic as a function of the fundamental component of the BEMF. In both cases the 13<sup>th</sup> harmonic is shown in pu of the fundamental component of the BEMF. This normalization compensates for the effects due to the variation of the average temperature. It is observed from Fig. 6 that for the case of a constant magnet temperature distribution, the relative magnitude of the 13<sup>th</sup> harmonic is almost insensitive to the variations of the mean magnet temperature and of the fundamental component of the BEMF. On the contrary, it is observed for the case of the non-uniform magnet temperature distribution, that the 13<sup>th</sup> harmonic magnitude increases with the mean magnet temperature, as well as with the magnitude of the fundamental component of the BEMF. Consequently, the pu value of the 13<sup>th</sup> harmonic decreases as  $T_{max} - T_{min}$  increases. The different behavior of the 13<sup>th</sup> harmonic for the case of a uniform and a non-uniform temperature distribution can be potentially used to estimate the differential temperature due to a non-uniform magnet temperature distribution.

Fig. 7 shows the 13<sup>th</sup> harmonic component magnitude vs. the differential magnet temperature, i.e.  $T_{max} - T_{min}$ , for the case of non-uniform temperature distribution. It is seen to change almost linearly with the differential temperature. This relationship can be used to estimate  $T_{max} - T_{min}$ , which combined with the mean PM temperature,  $T_r$ , can be used to estimate the magnet temperature distribution from (18). It was shown in the previous subsection that  $T_r$  can be estimated either by injecting a high frequency signal (see Fig. 5 and (10)), or from the fundamental component of the BEMF (see Fig. 4 and (17)). It is finally noted that although the 13<sup>th</sup> harmonic of the BEMF has been used in the preceding discussion, the -11<sup>th</sup> harmonic was observed to have a similar behavior. Though higher order

$P_R$ [kW]	$V_R$ [V]	$I_R$ [A]	$f_R$ [rpm]	P
7.5	300	14.5	1000	6

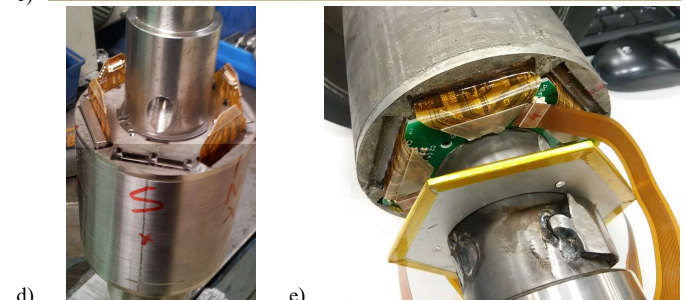
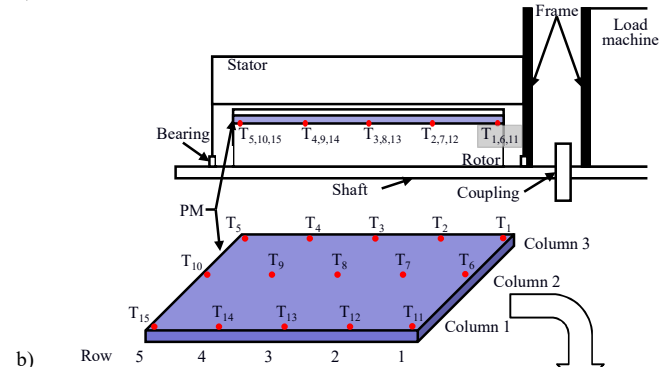
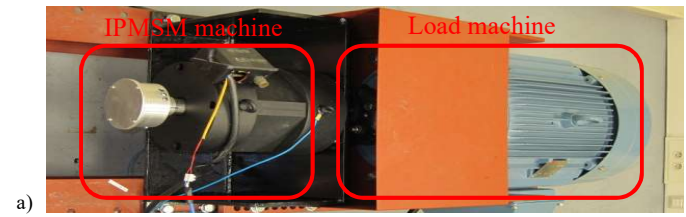


Fig. 8.- Experimental test bench (IPMSM), a), thermocouples location, b), flexible PCB, c), rotor assembling, d), and assembled rotor, e).



Fig. 9.- Thermal Insulation coat

harmonics could also potentially be used, the magnitude of the voltage harmonic decreases with the harmonic order. This results in a reduction of the signal-to-noise ratio, therefore compromising the accuracy of the method. A mathematical model linking the

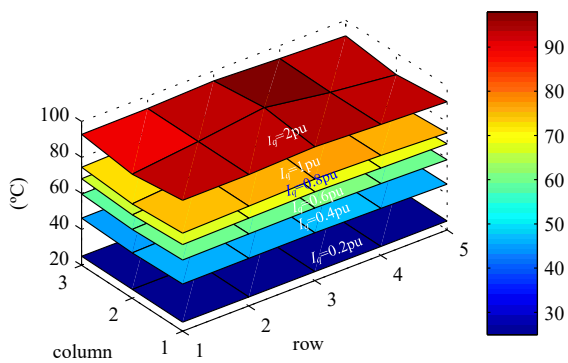


Fig. 10.- Experimentally measured magnet temperatures for  $I_{dq}$  current of: 0.2, 0.4, 0.6, 0.8, 1 and 2 pu.  $I_d=0$  pu,  $\omega_r = 2*\pi*50$  rad/s (1pu).

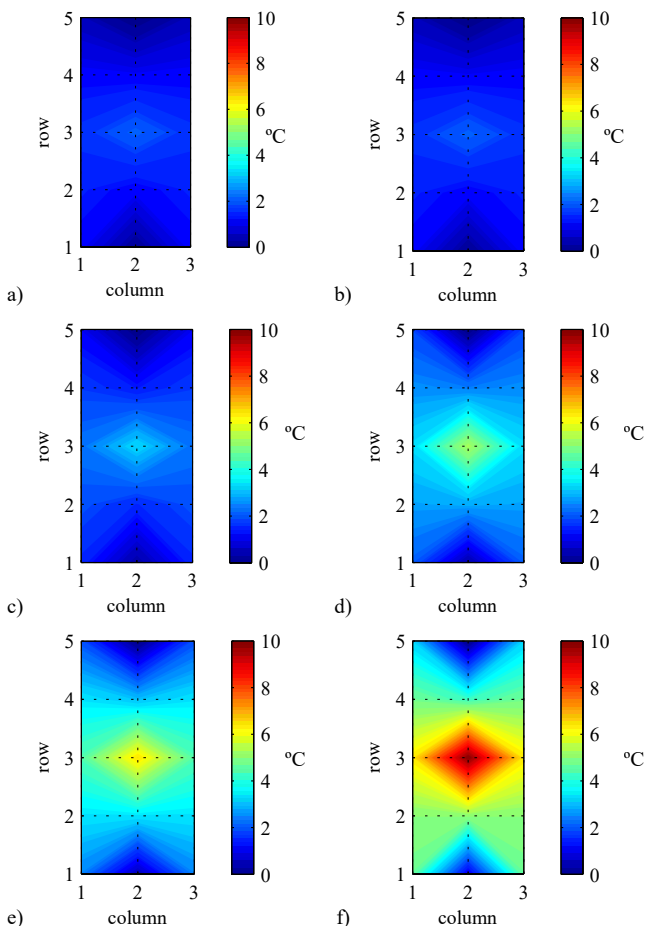


Fig. 11.- Experimentally measured magnet differential temperature, for the experimental results shown in Fig. 10. Sensor  $T_{10}$  (see Fig. 8), is used as the base temperature.  $I_q = 0.2$  pu, a), 0.4 pu, b), 0.6 pu, c), 0.8 pu, d), 1 pu, e), and 2 pu, f).

PM temperature spatial distribution and the BEMF harmonic content to explain the behavior observed in Fig. 6 and 7 is currently being developed.

#### IV. Temperature measurement

Verification of the proposed concepts will require measurement of the PM temperature distribution. Sensors setup reported in the literature [5-7, 9] for this purpose has limited spatial resolution. Among these, the highest resolution was provided by the system described in [7], in which the rotor

was equipped with 13 thermocouples located along one PM. This allows the measurement of the temperature along one PM in the rotor axial direction, but not in the tangential direction, being therefore inadequate for the analysis presented in this paper.

The proposed method has been tested on an IPMSM (see Fig. 8a) the same design as in simulations was used (see Fig. 1). The machine parameters are shown in Table II. A 2D sensor array has been used to measure the IPMSM PM temperature in the axial and tangential directions. It consists of an array of 3x5 I<sup>2</sup>C temperature sensors (see Fig. 8b), which are mounted on flexible PCBs, as shown in Fig. 8c, and further attached to each magnet. Fig. 8d shows the flexible PCBs during rotor assembling, every magnets being equipped with a sensor array. All the PCBs are connected to a “connection PCB” (see Fig. 8e). The measured temperatures are transmitted via a *Wi-Fi* link. More details can be found in [22].

Experimental results including uniform and non-uniform magnet temperature distributions will be shown. For the uniform magnet temperature experiments, the machine is heated up by injecting  $i_{dq}$  current. The injection of fundamental current will produce non-uniform magnet temperature distribution [7]. To achieve a uniform magnet temperature distribution, the fundamental current is removed, the machine being covered with a thermal insulating coat (see Fig. 9). During this process, the load machine is used to maintain the test machine rotating at its rated speed. Measurements from the sensors indicate that the temperature becomes uniform  $\approx 12$  min after the  $i_{dq}$  excitation was removed, the BEMF being then measured.

Fig. 10 shows the PM temperature measured by the 3x5 sensor array, when  $I_q$  current changes from 0 to 1pu in steps of 0.2pu and for  $I_d=2$ pu (2pu overload). No  $d$ -axis current was injected ( $I_d=0$ ), MTPA is not implemented therefore. Consequently, observed temperature variations are due exclusively to the  $q$ -axis current. For each operating condition, the temperature is measured 30 min. after  $I_q$  is established. This time was seen to be enough for the machine to reach its steady state thermal condition. As expected, the magnet temperature increases with  $I_q$ . It is also observed that the magnet temperature is not uniform, being higher at the central area, the risk of demagnetization being therefore higher in this region. It is also observed that temperatures measured by sensors in row 1 are a little bit higher than for sensors in row 5. Row 1 is the closest to the mechanical coupling with the load machine, (see Fig. 8a-b). The heat transfer between the IPMSM and the load IM through the mechanical coupling could cause this effect.

Fig. 11 shows the differential temperature for the experimental results shown in Fig. 10. Temperature measured by sensor  $T_{10}$  (see Fig. 8) is used as the base temperature, as it always exhibits the lowest temperature.

It can be observed that the bigger the  $I_q$  current is, the bigger the differential temperatures are. The maximum differential temperature without using  $d$ -axis current is  $\approx 9.92$  °C. It is noted that the stack length of the test machine is 100mm; higher temperature variations would be therefore expected in larger machines.

Finally, Fig. 12 shows the magnet differential temperature for a speed of  $\omega_r = 1.7$ pu, which is the maximum operating speed of the

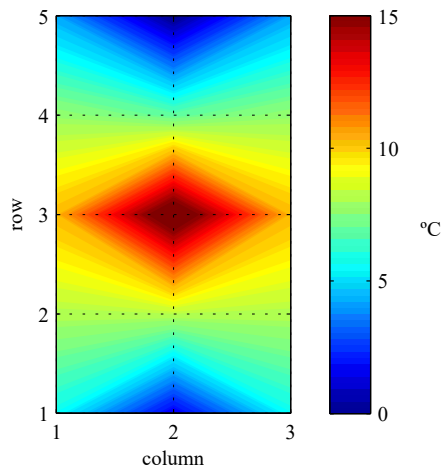


Fig. 12.- Experimentally measured magnet differential temperature.  $I_d=0.9$  pu,  $I_q=1$  pu,  $\omega_r=2*\pi*85$  Hz (1.7 pu).

test machine, with  $I_d=1$  pu and  $I_q=0.9$  pu, i.e. deep flux-weakening operation. The maximum differential temperature in this working condition is  $\approx 15$  °C.

It is finally noted that the system shown in Fig. 8 allows measuring the temperature distribution in all the six rotor magnets (see Fig. 8d and 8e). No significant differences among magnets of the PM temperature distributions have been observed. Consequently, the experimental results shown in Fig. 10-12 are limited to only one PM.

## V. Experimental results

For the experimental verification, 1200V, 100A IGBT power modules were used. Symmetric sine-triangle PWM with triplen harmonic injection was used. It is noted that the switching pattern in this case is the same as for conventional SVM. The switching frequency was 10 kHz. Use of the method with the inverter operating in the overmodulation region or in six-step has not been studied yet.

### a) Mean magnet temperature estimation ( $T_r$ )

Fig. 13a shows the BEMF for the case of  $\omega_r=1$  pu, the BEMF being obtained from the fundamental current controller output. Non-linear behavior of the inverter, i.e. dead-time, turn-on/turn-off time and voltage drop on the diodes and power switches,... need to be decoupled from the fundamental current controller output to estimate the machine BEMF or the rotor high frequency resistance. For the present research, the method proposed in [23] (also used in [5]) was used since this method has reduced complexity. Fig. 13b and 13c show the FFT of the BEMF for the case of uniform and non-uniform magnet temperature distributions respectively. Magnitudes are normalized in pu with respect to the fundamental component of the BEMF, a logarithmic scale being used.

Fig. 14 and 15 show the magnitude of the fundamental component of the BEMF and the estimated rotor  $d$ -axis high frequency resistance respectively, as a function of the mean magnet temperature (see Table III). Both the fundamental component of the BEMF and the estimated  $d$ -axis high frequency resistance, are seen to change almost proportional to the mean PM temperature. Consequently, both terms can be used to estimate the mean PM temperature, which is consistent

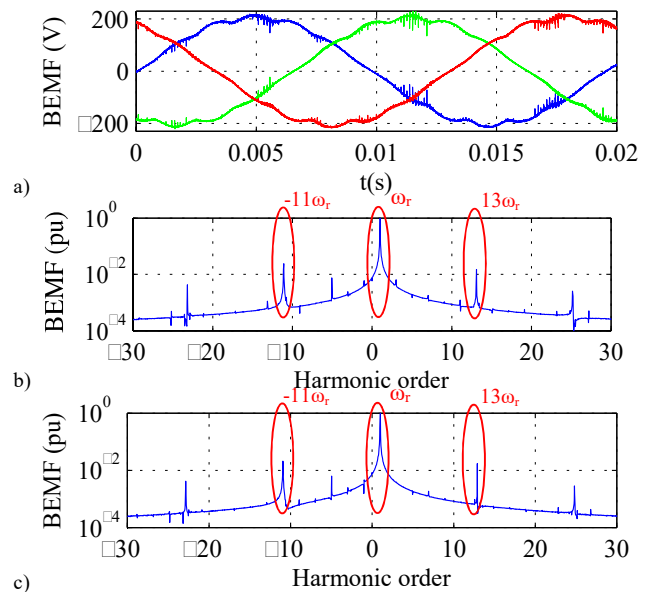


Fig. 13.- BEMF, a), and BEMF frequency spectrum for uniform magnet temperature distribution, b), and non-uniform magnet temperature distribution, c).  $I_d=I_q=0$  pu and  $\omega_r=2*\pi*50$  rad/s.

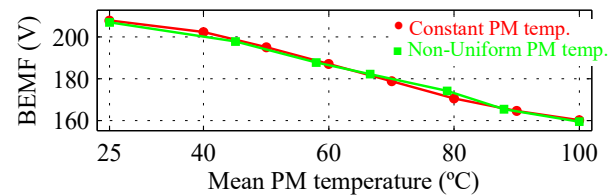


Fig. 14.- Fundamental component of the BEMF vs. mean magnet temperature for the case of uniform and non-uniform temperature distributions.  $\omega_r=2*\pi*50$  rad/s.

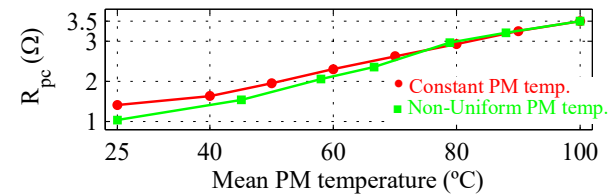


Fig. 15.- Estimated  $d$ -axis high frequency resistance for the case of uniform and non-uniform temperature distributions. Pulsating  $d$ -axis high frequency current injection,  $\omega_{hf}=2*\pi*250$  rad/s,  $I_{hf}=0.05$  pu.  $I_d=I_q=0$  pu and  $\omega_r=2*\pi*50$  rad/s.

with the simulation results shown in Fig. 4 and 5. It is also observed that the differences both in the fundamental component of the BEMF (Fig. 14) and high frequency resistance (Fig. 15) for the case of a uniform and non-uniform temperature distributions are very small or even negligible. Consequently, the use of these terms for differential PM temperature estimation is not viable.

### b) Differential magnet temperature estimation

Fig. 16a shows the magnitude of the BEMF 13<sup>th</sup> harmonic vs. PM temperature, both for the cases of uniform and non-uniform PM temperature distributions. Similarly, Fig 16b shows the magnitude of the BEMF 13<sup>th</sup> harmonic vs. the magnitude of the fundamental component of the BEMF. The minimum, maximum, and mean temperatures, i.e.  $T_{min}$ ,  $T_{max}$  and  $T_r$  for these experimental results are shown in Table III, the maximum differential temperature being  $\approx 15$ °C.

Uniform magnet temperature distribution		Non-uniform magnet temperature distribution			
Cases	$T_r(^{\circ}\text{C})$	Cases	$T_{max}(^{\circ}\text{C})$	$T_{min}(^{\circ}\text{C})$	$T_r(^{\circ}\text{C})$
#1	$\approx 100$	#1	$\approx 106.8$	$\approx 92.2$	$\approx 100$
#2	$\approx 90$	#2	$\approx 92.2$	$\approx 83.1$	$\approx 88.0$
#3	$\approx 80$	#3	$\approx 82.0$	$\approx 75.8$	$\approx 78.9$
#4	$\approx 70$	#4	$\approx 69.1$	$\approx 64.1$	$\approx 66.6$
#5	$\approx 60$	#5	$\approx 59.5$	$\approx 56.5$	$\approx 58.0$
#6	$\approx 50$	#6	$\approx 44.0$	$\approx 46.1$	$\approx 45.1$
#7	$\approx 40$	#7	$\approx 25.0$	$\approx 25.0$	$\approx 25.0$
#8	$\approx 25$				

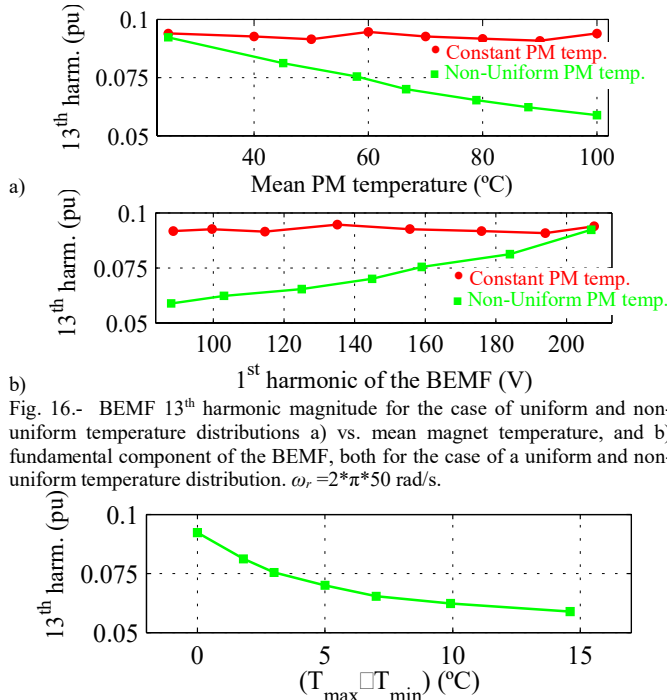


Fig. 17.- BEMF 13<sup>th</sup> harmonic magnitude vs. differential magnet temperature  $T_{max}-T_{min}$ .  $\omega_r=2*\pi*50$  rad/s (1pu).

Experimental results shown in Fig. 16 are in good agreement with simulation results shown in Fig. 6, confirming the usefulness of the 13<sup>th</sup> harmonic of the BEMF for differential PM temperature estimation purposes.

Fig. 17 shows the magnitude of the BEMF 13<sup>th</sup> harmonic variation vs. the differential magnet temperature for the non-uniform PM temperature distribution case. This relationship being consistent with the simulation results (see Fig 7), a remarkable agreement between simulation and experimental results being observed in general.

### c) Magnet temperature distribution estimation

Fig. 18a-f shows the magnet temperature estimation error for the experimental results shown in Fig. 10-11. The mean PM temperature is estimated either from the fundamental component of the BEMF or the estimated  $d$ -axis high frequency resistance, see Fig. 14 and 15. High frequency signal injection based temperature estimation methods are typically used for zero or low speed operation, since the induced BEMF is very small in this case. On the contrary, in the mid-to-high speed region, BEMF based methods are preferred as they provide good accuracy and do not required

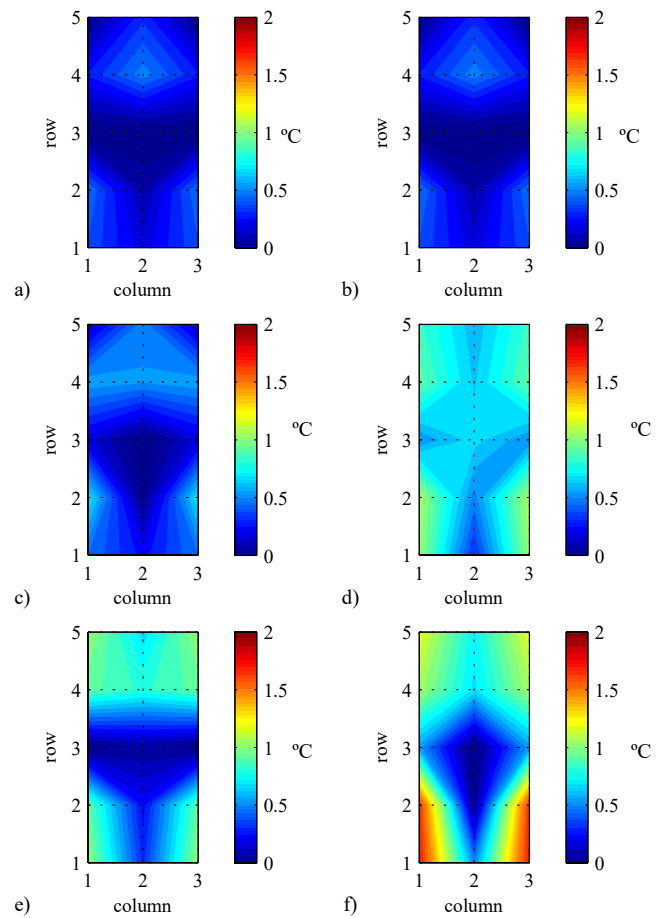


Fig. 18.- Temperature estimation error for the same experimental results that are shown in Fig. 10 and 11.

injection of an additional signal. BEMF has been used for the experimental results shown in Fig. 18. The differential temperature,  $T_{max}-T_{min}$ , is estimated from the 13<sup>th</sup> harmonic of the BEMF, see Fig. 17. The estimation error in Fig. 18 is the difference between the measured temperatures and the estimated temperatures using (18). It is observed that the maximum temperature estimation error is  $<1.75^{\circ}\text{C}$  (Fig. 18f) and occurs in an overloaded condition, with i.e.  $I_q=2$  pu. It is also observed that the maximum temperature estimation errors occur at the magnet corners. Although FEA magnet temperature distribution color maps are not shown, this effect was not predicted by FEA. This issue is under ongoing research. It is also observed that the temperature estimation error is not symmetric in the axial direction with respect to the center of the magnet (row 3). This asymmetry is believed to be due to the heat transfer between the IPMSM and the load IM through the mechanical coupling, see Fig. 8.

Finally, Fig. 19 shows experimental results for the IPMSM test machine with both torque and speed varying from zero to their corresponding rated value in steps of 0.1 pu. The  $d$ -axis current was set to zero below rated speed, i.e.  $I_d=0$  for  $\omega_r < 1$ pu. Field weakening (i.e.  $I_d \neq 0$ ) was used for  $\omega_r > 1$ pu.

Fig. 19a and 19b show the measured mean and maximum magnet differential temperature maps. It is observed that both increase with load (i.e.  $I_q$  current), which is consistent with the

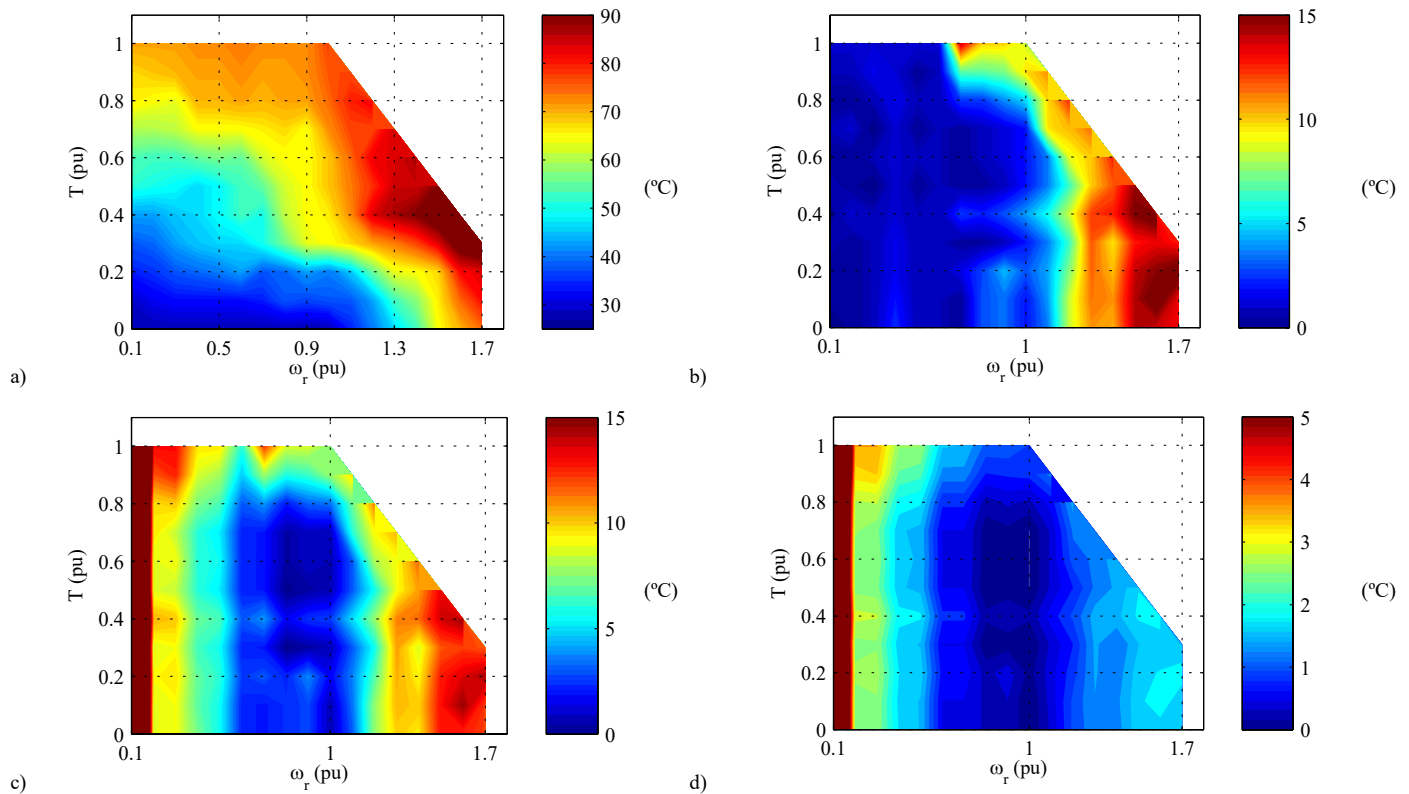


Fig. 19. Experimental results. a) Measured magnet temperature, b) measured maximum magnet differential temperature  $T_{max}-T_{min}$ , c) estimated maximum magnet differential temperature and d) estimated maximum magnet differential temperature error.

experimental results shown in Fig. 10 and 11, and speed, which is due to the increase of the eddy-current and hysteresis losses with frequency; the highest differential temperature occurs in the flux-weakening region.

Fig. 19c and 19d show the maximum differential magnet temperature estimation and the maximum temperature error respectively. The differential temperature was estimated from the 13<sup>th</sup> harmonic of the BEMF. As expected, the maximum temperature estimation error occurs in the low speed region due to the reduced magnitude of the BEMF (fundamental component and harmonics) at low speed. The estimation error is seen to quickly decrease as the speed increases, being smaller than  $\approx 2$  °C for speeds  $>0.35$  pu.

It is noted that the proposed methods is only applicable provided that the frequency of the BEMF harmonic being analyzed is below the Nyquist frequency of the control. For the experimental results provided in this paper, the maximum speed is 85Hz, i.e. the maximum frequency of the 13<sup>th</sup> harmonic component is at 1105 Hz, well below the Nyquist frequency (5 kHz).

It is finally noted that all the experimental results presented in this section were obtained with the machine operating in steady-state. If changes in the machine temperature occur, a delay of  $\approx 2.5$ ms exists in the temperature estimation due to the signal processing. This delay is considered negligible compared with the machine thermal time constant.

## VI. Conclusions

This paper proposes a method to estimate the PM spatial temperature distribution in PMSMs. The method requires estimation of the mean and differential PM temperature. Mean PM

temperature can be estimated using either the fundamental component of the BEMF or injecting a pulsating  $d$ -axis high frequency current signal and measuring the  $d$ -axis high frequency resistance. The differential PM temperature is estimated using higher order harmonics of the BEMF. The method is applicable to IPMSMs; extension of the method to SPMSMs or other machine designs has not been evaluated yet. The proposed method was developed on an empirical basis. Development of a mathematical model is ongoing. The principles of the method as well as simulation and experimental results have been presented to demonstrate its viability.

## VII. Appendix: Magnet Temperature Estimation Using The High Frequency Resistance

The high frequency model of a PMSM is described by (1). The  $d$  and  $q$ -axis components of the high frequency resistances,  $R_{d\text{hfr}}$  and  $R_{q\text{hfr}}$ , are function of both the stator and rotor high frequency resistances (18), where  $R_{\text{hf}}$  ( $d$  or  $q$ -axis) is the high frequency resistance seen from the stator terminals,  $R_{\text{shf}}$  ( $d$  or  $q$ -axis) is the stator high frequency resistance and  $R_{\text{rhf}}$  ( $d$  or  $q$ -axis) is the stator-reflected rotor high frequency resistance. Stator ( $R_{\text{shf}(T_s)}$ ) and rotor ( $R_{\text{rhf}(T_r)}$ ) resistances are affected by the corresponding stator ( $T_s$ ) and rotor ( $T_r$ ) temperatures as shown by (19), where  $\alpha_{cu}$  is the copper thermal resistive coefficient (which affects to the stator high frequency resistance),  $\alpha_{mag}$  is the magnet thermal resistive coefficient (which affects to the rotor high frequency resistance),  $T_0$  is the room temperature,  $R_{\text{shf}(T_0)}$  is the stator resistance at the room temperature and  $R_{\text{rhf}(T_0)}$  is the rotor resistance at the room temperature [5-7]. The magnet temperature can be estimated

from (20), knowledge of the high frequency resistance of the machine at the room temperature and of the stator temperature being required.

$$R_{hf} = R_{shf} + R_{rhf} \quad (18)$$

$$R_{hf} = R_{hf(T_s, T_r)} = R_{shf(T_s)} + R_{rhf(T_r)} = R_{shf(T_0)}(1 + \alpha_{cu}(T_s - T_0)) + R_{rhf(T_0)}(1 + \alpha_{mag}(T_r - T_0)) \quad (19)$$

$$T_r = T_0 + \frac{R_{hf(T_s, T_r)} - R_{shf(T_0)}(1 + \alpha_{cu}(T_s - T_0)) - R_{rhf(T_0)}}{\alpha_{mag} R_{rhf(T_0)}} \quad (20)$$

## VIII. References

- [1] M. Kamiya, Y. Kawase, Y. Kosada and N. Matsui, "Temperature distribution analysis of permanent magnet in interior permanent magnet synchronous motor considering PWM carrier harmonics," IEEE-ICEMS, pp. 2023–2027, Oct. 2007.
- [2] P. Milanfar and J. H. Lang, "Monitoring the thermal condition of permanent-magnet synchronous motors," IEEE Trans. on Aerospace and Electronic Systems, 32(4): 1421-1429, Oct. 1996.
- [3] N. Bianchi and T. M. Jahns "Design, analysis, and control of interior PM synchronous machines," Tutorial Course Notes, IEEE-IAS'04, Oct. 2004.
- [4] J. F. Gieras and M. Wing, "Permanent magnet motor technology: design and application". Second edition 2002.
- [5] D. Reigosa, F. Briz, P. Garcia, J. M. Guerrero and M. W. Degner, "Magnet temperature estimation in surface PM machines using high frequency signal injection". IEEE Trans. on Ind. Appl., 46(4): 1468–1475, July-Aug. 2010.
- [6] D. Reigosa, F. Briz, M. W. Degner, P. Garcia and J. M. Guerrero, "Magnet temperature estimation in surface PM machines during six-Step operation". IEEE Trans. on Ind. Appl., 48(6): 2353–2361, Nov.-Dec. 2012.
- [7] D. Reigosa, D. Fernandez, H. Yoshida, T. Kato and F. Briz "Permanent magnet temperature estimation in PMSMs using pulsating high frequency current injection," IEEE Trans. on Ind. Appl., 51(4): 3159–3168, July-Aug. 2015.
- [8] M. Ganchev, C. Kral and T. Wolbank, "Compensation of speed dependency in sensorless rotor temperature estimation for permanent-magnet synchronous motors," IEEE Trans. on Ind. Appl., 49(6): 2487-2495, Nov.-Dec. 2013.
- [9] M. Ganchev, C. Kral, H. Oberguggenberger and T. Wolbank, "Sensorless rotor temperature estimation of permanent magnet synchronous motor," IEEE IECON, pp. 2018-2023, Nov. 2011.
- [10] A. M. El-Refai, N. C. Harris, T. M. Jahns, K. M. Rahman, "Thermal Analysis of Multibarrier Interior PM Synchronous Machine Using Lumped Parameter Model". IEEE Trans. on Energy Conv., 14(2): 303–309, June 2004.
- [11] C. Kral, A. Haumer and S. B. Lee, "A Practical Thermal Model for the Estimation of Permanent Magnet and Stator Winding Temperatures". IEEE Trans. on Pow. Elect., 29(1): 455–464, Jan. 2014.
- [12] Z. J. Liu, K. J. Binns, T. S. Low, "Analysis of Eddy current and thermal problems in permanent magnet machines with radial-field topologies". IEEE Trans. on Mag., 31(3): 1912–1915, May. 1995.
- [13] A. J. Grobler, S. R. Holm and G. van Schoor, "Thermal modelling of a high speed permanent magnet synchronous machine". IEEE-IEMD, pp.319–324, May. 2013.
- [14] T. Huber, W. Peters and J. Böcker, "A Low-Order Thermal Model for Monitoring Critical Temperatures in Permanent Magnet Synchronous Motors". IET-PEMD, pp. 1–6, April 2014.
- [15] <https://www.jmag-international.com>
- [16] K. Liu and Z. Q. Zhu "Online estimation of the rotor flux linkage and voltage-source inverter nonlinearity in permanent magnet synchronous machine drives," IEEE Trans. on Pow. Elect., 29(1): 418-427, Jan. 2014.
- [17] K. Liu and Z.Q. Zhu "Mechanical Parameter Estimation of Permanent Magnet Synchronous Machines with Aiding from Estimation of Rotor PM Flux Linkage", IEEE Trans. on Ind. Appl., 51(4): 3115–3125, July-Aug. 2015.
- [18] S. Underwood, and I. Husain, "On-line parameter estimation and adaptive control of permanent magnet synchronous machines," IEEE Trans. Ind. Electron., 57(7): 2435-2443, Jun. 2010.
- [19] S. Ichikawa, M. Tomita, S. Doki, and S. Okuma, "Sensorless control of permanent-magnet synchronous motors using online parameter identification based on system identification theory," IEEE Trans. Ind. Electron., 53(2): 363-372, Apr. 2006.
- [20] S. Ruoho, J. Kolehmainen, J. Ikaheimo and A. Arkkio, "Interdependence of demagnetization, loading, and temperature rise in a permanent-magnet synchronous motor," IEEE Trans. Mag., 46(3): 949–953, Mar. 2010.
- [21] A. Specht, O. Wallscheid, J. Bocker, "Determination of rotor temperature for an interior permanent magnet synchronous machine using a precise flux observer," IEEE IPEC, pp. 1501–1507, May 2014.
- [22] D. Fernandez, D. Reigosa, T. Tanimoto, T. Kato and F. Briz, "Wireless Permanent Magnet Temperature & Field Distribution Measurement System for IPMSMs", IEEE-ECCE'15, pp. 3996-4003, Sep. 2015.
- [23] J. M. Guerrero, M. Leetmaa, F. Briz, and R. D. Lorenz, "Inverter non-linearity effects in high-frequency signal-injection-based sensorless con- trol methods," IEEE Trans. Ind. Appl., vol. 41, no. 2, pp. 618–626, Mar./Apr. 2005.
- [24] A. Specht and L. Backer, "Observer for the Rotor Temperature of IPMSM," in International Power Electronics and Motion Control Conference (EPE/PEMC), 2010.
- [25] O. Wallscheid, T. Huber, W. Peters, J. Böcker, "Real-Time Capable Methods to Determine the Magnet Temperature of Permanent Magnet Synchronous Motors - A Review ," IEEE-IECON'14, pp. 811-818, Nov. 2014.